

Anti-Parity-Time Symmetry in a Su-Schrieffer-Heeger Sonic Lattice

Bolun Hu,^{1,2} Zhiwang Zhang,^{1,*} Zichong Yue,¹ Danwei Liao¹,, Yimin Liu,¹ Haixiao Zhang¹,
Ying Cheng,^{1,†} Xiaojun Liu^{1,3,‡}, and Johan Christensen^{4,§},

¹*Department of Physics, MOE Key Laboratory of Modern Acoustics, Collaborative Innovation Center of Advanced Microstructures, Nanjing University, Nanjing 210093, China*

²*School of Science, Jiangsu Provincial Research Center of Light Industrial Optoelectronic Engineering and Technology, Jiangnan University, Wuxi 214122, China*

³*College of Aerospace Engineering, Chongqing University, Chongqing 400044, China*

⁴*IMDEA Materials Institute, Calle Eric Kandel, 2, 28906 Getafe, Madrid, Spain*



(Received 14 January 2023; accepted 6 July 2023; published 7 August 2023)

The Su-Schrieffer-Heeger (SSH) model is an important cornerstone in modern condensed-matter topology, yet it is the simplest one-dimensional (1D) tight binding approach to dwell into the characteristics of spinless electrons in chains of staggered bonds. Moreover, the chiral symmetry assures that its surface-confining states pin to zero energy, i.e., they reside midgap in the energy dispersion. Symmetry is also an attribute related to artificial media that are subject to parity \mathcal{P} and time-reversal \mathcal{T} operations. This non-Hermitian family has been thoroughly nourished in a wave-based context, where anti- \mathcal{PT} (\mathcal{APT}) symmetric systems are the youngest belonging members, permitting refractionless optics, inverse \mathcal{PT} -symmetry breaking transition, and asymmetric mode switching. Here, we report the first extension of \mathcal{APT} symmetry in an acoustic setting by endowing a SSH lattice with gain and loss components. We show that the in-gap topological defect state hinges on the non-Hermitian phase, in that the broken symmetry suppresses it, yet when \mathcal{PT} or \mathcal{APT} symmetry is intact, it is observed with either damped or evanescent decay, respectively. Our experiments showcase how the non-Hermitian SSH lattice serves as a utile platform to investigate topological properties across various \mathcal{PT} symmetric phases using sound.

DOI: [10.1103/PhysRevLett.131.066601](https://doi.org/10.1103/PhysRevLett.131.066601)

Systems respecting space-time reflection symmetry have been synthesized using gain and loss profiles in man-made materials. Owing to their broad implications in both science and technology, these \mathcal{PT} symmetric metamaterials and lattices remain an active area in quantum physics, optics, acoustics, plasmonics, etc. [1–5]. Loss, the often regarded unfavorable non-Hermitian ingredient, has lately been put in a more advantageous spotlight, particularly in combination with its time-reversed image, that is, the gain counterpart. Beyond the phase where these two components only cancel each other out, at a certain gain-loss contrast, the threshold is reached at which the complex eigenvalues coalesce, yet even higher-order or encircling exceptional points have been reported [6–8]. This non-Hermitian avenue has lately been even further enriched by adding topology to the picture. Governed by the conventional bulk-boundary correspondence (BBC), the Hermitian nontrivial band topology determines the presence of localized interface states. However, the absence of Hermiticity not only alters the BBC, but also localizes the bulk states at the interfaces in the guise of skin states [9,10]. Other combinations of topology and non-Hermiticity have led to topological robust lasers [11,12], non-Hermitian second-order topological corner states [13,14], and a wealth of theory explaining the pivotal interplay between gain and

loss and their geometrical arrangements [15]. It is worth noting that non-Hermitian topology stems from early advances in condensed matter physics [16], yet, facile fabrications and a high degree of tunability has pushed forward significant headway in analogous acoustic and photonic settings [17,18].

Parity-time (\mathcal{PT}) and anti-parity-time (\mathcal{APT}) symmetry refer to the symmetry and antisymmetry with respect to the simultaneous action of the parity-inversion \mathcal{P} and time reversal symmetry operators \mathcal{T} . Mathematically, properties associated with \mathcal{PT} symmetry conjugate with the ones of \mathcal{APT} symmetry as their Hamiltonians only differ by an imaginary unit. Therefore, while \mathcal{PT} symmetric Hamiltonians commute with the joint parity-time operator, the \mathcal{APT} Hamiltonians anticommute with it. The stringent requisite to realize \mathcal{PT} symmetry demands balanced gain and loss units, whereas the implementation of the \mathcal{APT} counterpart is somewhat eased, yet elaborate experiments on the basis of positive-negative index stacks, cold atomic lattices, flying atoms, electrical circuits, and optical fibers have rendered the observation possible [19–23]. What remains elusive is to add the notion of topology in the context of a \mathcal{APT} symmetric phase [24], as this combination will unearth even more unusual topological wave characteristics, both in the presence and the absence of

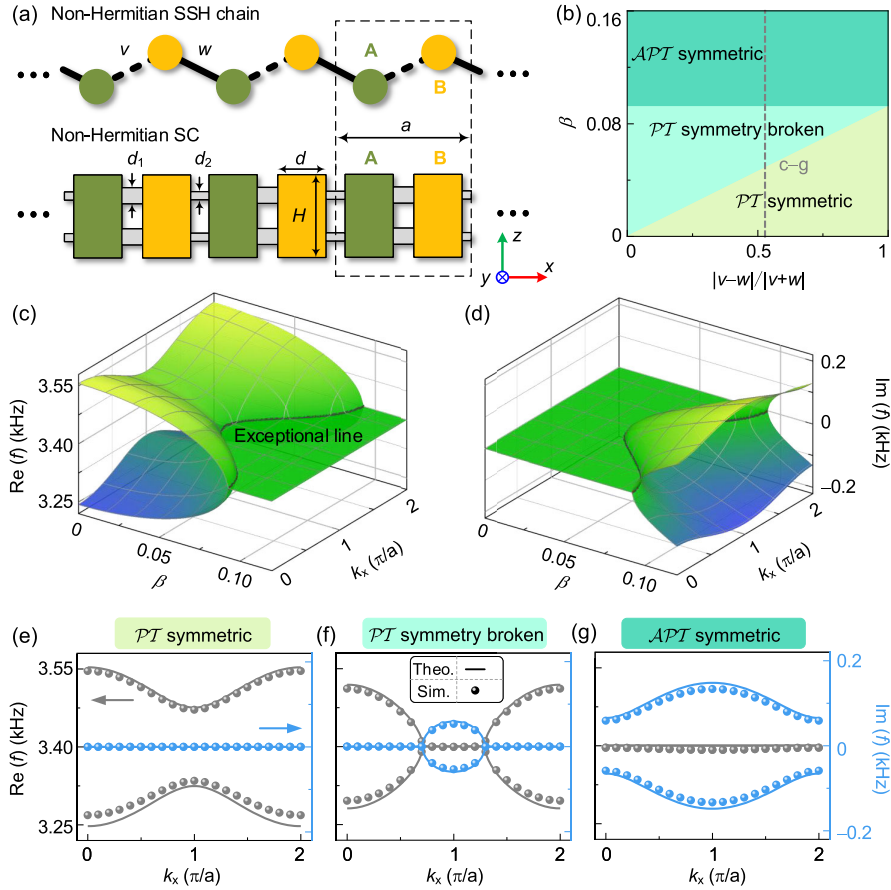


FIG. 1. Non-Hermitian phase diagram. (a) Schematics of the non-Hermitian SSH chain and corresponding SC composed of the coupled sublattices A and B . (b) Non-Hermitian phase diagram of the SSH chain while modulating the non-Hermiticity and coupling strengths. (c),(d) Real (c) and imaginary (d) band diagrams calculated by varying the non-Hermiticity factor β with $|v - w|/|v + w| = 0.5287$ as highlighted in (b). (e)–(g) Theoretical and simulated band diagrams with $\beta = 0.02$ (e), 0.06 (f), and 0.10 (g) in the $\mathcal{P}T$ symmetric, $\mathcal{P}T$ symmetry broken and $\mathcal{A}PT$ symmetric phases, respectively. In (c)–(g), the ratio of coupling strength is fixed at $|v - w|/|v + w| = 0.5287$ as highlighted by the gray dashed line in (b).

this unfamiliar non-Hermitian symmetry. Here, we construct a non-Hermitian SSH model by 3D printing connected cavities to emulate an implementation using sound waves. The acoustic SSH lattice is inherently lossy due to visco-thermal wall losses, fortunately, by adequately modulated thermoacoustic gain using carbon nanotube (CNT) films, we are able to endow the lattice with controllable gain and loss constituents. Our findings demonstrate an in-gap state of topological origin across the entire non-Hermitian phase spectrum. Unlike laterally confining edge states, damped or evanescently confined defect states are spawned in direct dependence of the non-Hermitian space-time reflection symmetry.

Non-Hermitian SSH model and its phase transition.— We begin from a 1D non-Hermitian SSH chain, which is composed of on-site loss and gain components [A and B , respectively, see Fig. 1(a)] coupled through intracell-intercell hopping amplitudes v/w . In an analog acoustic setting, as seen in the lower panel of Fig. 1(a), we utilize waveguide-connected cavities that constitute the 1D

non-Hermitian sonic crystal (NHSC). The acoustic hopping is mimicked by parallel waveguides of width d_1 and d_2 , positioned at $H/4$ and $3H/4$, respectively, according to the resonator height. We employ a metamaterials approach comprising effective parameters to add non-Hermiticity to the NHSC, in that the complex mass density is defined as $\rho_A = (1 - i\beta)\rho_0$ for the loss components, and $\rho_B = (1 + i\beta)\rho_0$ for the gain counterpart, while the bulk modulus is κ_0 . The value of β controls the amount of the gain or loss, and ρ_0 and κ_0 represent the parameters for air (see Supplemental Material Sec. I [25]). Consequently, the non-Hermitian Hamiltonian of our system (see Supplemental Material Sec. II [25] for the detailed derivation from acoustic motion equations) is expressed as

$$H_a(k) = H_e(k) + f_0\sigma_0, \quad (1)$$

with

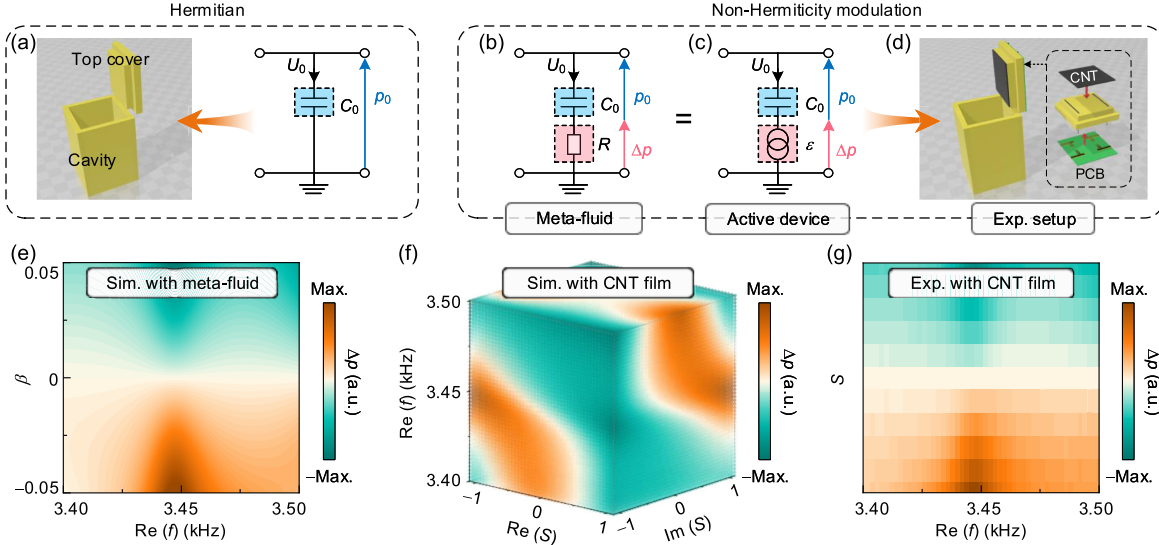


FIG. 2. Non-Hermiticity modulation in an acoustic cavity. (a) Structural schematic and the effective lumped-circuit model of a Hermitian acoustic cavity. (b) Effective lumped-circuit models where the non-Hermiticity is introduced through a metafluid, which is experimentally realized (c),(d) thanks to an active CNT lid coating. (e),(f) Simulated spectral amplitude modulation Δp vs the non-Hermiticity factor β of the metafluid (e), and vs the electrical signal modulation S applied to the CNT film (f). (g) Corresponding detected pressure modulation spectrum with the electrical signal strength from (f).

$$H_e(k) = \begin{bmatrix} -if_0\beta/2 & v + we^{-ika} \\ v + we^{ika} & if_0\beta/2 \end{bmatrix}, \quad (2)$$

where σ_0 denotes the 2×2 identity matrix, f_0 is the resonance frequency, and a represents the lattice constant. In the Hermitian case ($\beta = 0$), the Hamiltonian is symmetric under both parity \mathcal{P} ($\sigma_x, k \rightarrow -k$) and time reversal \mathcal{T} ($i \rightarrow -i, k \rightarrow -k$) operations with $\sigma_{x,y,z}$ for the Pauli matrices. On the contrary, adding a lossy or amplifying non-Hermitian channel ($\beta \neq 0$) breaks both \mathcal{P} and \mathcal{T} symmetry, yet, their combination, $\mathcal{PT} = \sigma_x, i \rightarrow -i$ preserves the symmetry, which means that the Hamiltonian in Eq. (2) commutes with \mathcal{PT} operation $[H_e, \mathcal{PT}] = 0$. On the other hand, the combination of chiral and time reversal symmetries suggests another operator, \mathcal{APT} , which satisfies $\mathcal{APT} = \sigma_z, i \rightarrow -i, k \rightarrow -k$ [30–32]. From Eq. (2), it can be proven that the Hamiltonian of the NHSC anticommutes with an \mathcal{APT} operation as $\{H_e, \mathcal{APT}\} = 0$. It is worthwhile to note that while the effective Hamiltonian remains always both \mathcal{PT} and \mathcal{APT} symmetric, β determines the symmetric phase of the eigenfunctions [33]. As a result, we are able to characterize the NHSC by different phases [as shown in Fig. 1(b)] according to the symmetry of the states as discussed in the following. By solving the eigenvalue equation $H_e\psi = \lambda\psi$ with the wave function ψ , we obtain the following eigenvalues:

$$\lambda(k) = \pm \sqrt{v^2 + w^2 + 2vw \cos(ka) - (f_0\beta/2)^2}, \quad (3)$$

which can be rewritten to acoustic frequencies $f = f_0 + \lambda$. Its solutions constitute a non-Hermitian phase diagram that displays three sections in dependence on the coupling ratio $|v - w|/|v + w|$ and β as shown in Fig. 1(b). The yellow zone marks the section of \mathcal{PT} symmetric eigenfunction, i.e., inside which all eigenvalues are simultaneously real for sufficiently small values of $\beta < 2|v - w|/f_0$ (see Supplemental Material Sec. III [25]). Beyond this section, for $2|v - w|/f_0 < \beta < 2|v + w|/f_0$, the sign of the radicand depends on the wave number k , which gives rise to \mathcal{PT} -symmetry broken eigenfunctions (light-green zone), of which some eigenvalues are real while others are complex. If the non-Hermiticity factor is further increased beyond the threshold $\beta > 2|v + w|/f_0$, the negative radicand gives rise to purely imaginary eigenvalues. It also implies a transition from the \mathcal{PT} symmetry broken into the intact \mathcal{APT} symmetric phase (dark-green zone). To expand on these phase transitions, in Figs. 1(c)–1(d) we illustrate the calculated real and imaginary band diagrams of the NHSC as a function of the added non-Hermiticity. The coalescence among the two-band dispersion takes place at the cavity resonance frequency f_0 in the form of an uneven exceptional line. As captured in Figs. 1(e)–1(g), the transition from intact, toward broken \mathcal{PT} symmetry, leads to the \mathcal{APT} symmetric phase, by virtue of vanishing (emerging) real (imaginary) eigenvalues. The simulated results exhibit good agreement with the theoretical ones. We emphasize that, although the coupling ratio is fixed at $|v - w|/|v + w| = 0.5287$ for the sake of simplicity in Figs. 1(c)–1(g), any generic points in the phase diagram of Fig. 1(b) obey the above-discussed rules (see Supplemental Material Sec. III [25]).

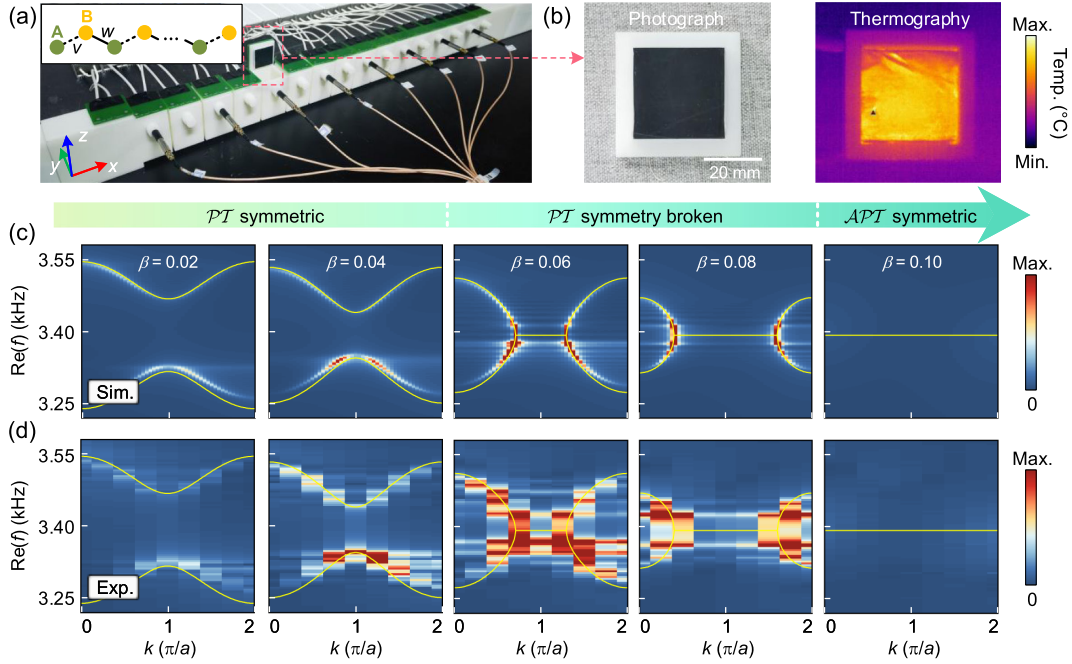


FIG. 3. Measured dispersion across various \mathcal{PT} symmetric phases. (a) Photograph of the experimental setup. The inset shows the arrangements of non-Hermitian sites in the finite NHSC. (b) CNT film mounted of the top lid of the cavity and its corresponding thermogram. (c),(d) Simulated (c) and experimentally measured (d) band diagrams with the non-Hermiticity factor β ranging from 0.02 to 0.10 as indicated. Yellow solid lines represent the theoretical results.

Modulating acoustic non-Hermiticity.—To realize the \mathcal{APT} symmetric NHSC, a relatively large non-Hermiticity factor is required that up until this point remains a challenging experimental undertaking. Here, we design an approach to attain the desired gain and loss factors, based on electrically activated CNT films. Figure 2(a) illustrates a Hermitian acoustic cavity, which could be considered as an acoustic capacitance C_0 using an effective lumped-circuit model. Thus, the pressure response can be derived as $p_0 = U_0(1/-i\omega C_0)$, where U_0 represents the volume velocity and ω is the angular frequency. Acoustic gain (loss), i.e., sound amplification (attenuation), is modeled thanks to a metafluid with the effective mass density as discussed earlier. In the lumped circuit model, it corresponds to an additional acoustic resistance R [Fig. 2(b)], which leads to the deterministic modulation of the pressure change Δp [Fig. 2(e)], compared with the Hermitian case. Gain (loss), therefore results in a pressure increment (drop), i.e., $\Delta p > 0$ ($\Delta p < 0$). Further, in the circuit model, this pressure modulation is accounted for through the electromotive force [\mathcal{E} , see Fig. 2(c)]. The experimental realization shown in Fig. 2(d), contains CNT film coating of the top lid of the acoustic cavity, which is connected with the electric circuit board via electrodes. With an appropriately applied time-varying current, the film operates as an acoustic active device thanks to the electrothermoacoustic coupling effect. By varying the amplitude and phase of the input current signal S , the frequency dependent pressure modulation Δp can be determined [Fig. 2(f)] to shape the range of the

accessible non-Hermitian component. These simulated current signals aid in obtaining the equivalent experimental spectrum of the acoustic non-Hermiticity modulation using CNT films, as shown in Fig. 2(g).

Experimental observation of non-Hermitian phase transitions.—In what follows, we expand on the afore-discussed phenomena by utilizing the non-Hermitian CNT coated cavities for the coveted non-Hermitian SSH chain. In Fig. 3(a), we show the fabricated finite 1D NHSC consisting of eight unit cells. The non-Hermiticity is precisely electrically modulated through the CNT film pasted on the top lid of each cavity as shown in Fig. 3(b). Also shown here is a thermography of the film when electrothermoacoustically activated. By steadily increasing the non-Hermiticity [dashed line across the phases in Fig. 1(b)], we aim at detecting the nontrivial dispersion comprising the \mathcal{PT} symmetric, \mathcal{PT} symmetry broken, and \mathcal{APT} symmetric phase transitions. To predict the real bands, we Fourier transform the detected acoustic pressure fields from each cavity numerically (using 48 unit cells), as rendered in Fig. 3(c) for five different values of β ranging from 0.02 to 0.10. In the same way, the experimental data are obtained and illustrated in Fig. 3(d). Additionally, we superimpose matching theoretical bands obtained from Eq. (3). In the \mathcal{PT} symmetric phase regime we observe a gapped dispersion ($\beta = 0.02, 0.04$). However, when the two bands coalesce along the uneven exceptional line [see Fig. 1(c)], we enter the \mathcal{PT} symmetry broken phase comprising finite sections in momentum space (along

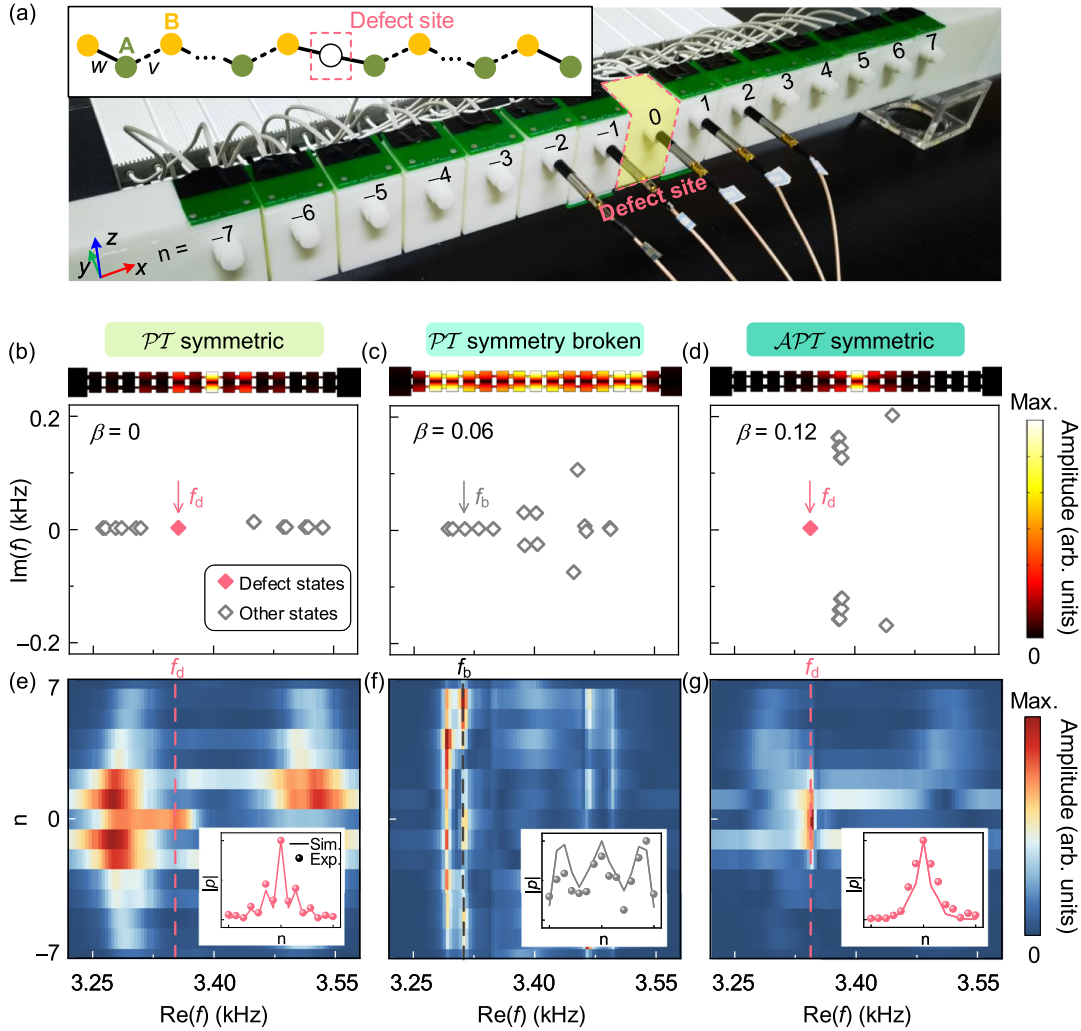


FIG. 4. Non-Hermitian topological in-gap defect state. (a) Photograph of the experimental setup with the introduced defect site, which is composed of a passive cavity as highlighted by the pink box. The inset shows the position of the introduced defect site in the finite NHSC. (b)–(d) Calculated eigenfrequencies of the NHSC in the \mathcal{PT} symmetric [$\beta = 0$, (b)], \mathcal{PT} symmetry broken [$\beta = 0.06$, (c)], and \mathcal{APT} symmetric phases [$\beta = 0.12$, (d)]. The insets show the pressure field distributions of the eigenstates marked in subfigures. (e)–(g) Frequency-dependent spatial profiles of the pressure amplitude fields measured in each cavity. Insets: magnifications of the defect and bulk states at the frequencies marked by the dashed lines.

the k axis) of flat vanishing real eigenfrequencies, $f = f_0$ ($\beta = 0.06, 0.08$). Beyond this curved section, entering the \mathcal{APT} symmetric phase, complete band degeneracy in momentum space takes place in the form of entirely flat dispersion. Here, we need to stress that the flat regimes beyond the uneven exceptional lines are challenging to observe experimentally due to their zero group velocity.

Non-Hermitian topological defect states.—By introducing an extra site into the middle of a Hermitian SSH chain, a topological interface is formed between two regions of different topological invariant, which gives rise to a topological in-gap defect state [34–36]. Taking non-Hermiticity into consideration, the topology can be characterized by the global Berry phase (see Supplemental Material Sec. V [25]). Then, we study its influence on the state confinement across all phases. As seen in Fig. 4(a), we

insert a defect site (index 0) at the center of a 14-units NHSC. In the Supplemental Material Sec. VI [25], we carefully deduce the eigenvalue problem of this non-Hermitian SSH lattice and we infer that $\mathcal{PT}/\mathcal{APT}$ symmetry is crucial to the appearance of the topological defect state, which ceases to exist in the \mathcal{PT} symmetry broken phase. To prove this, the simulated complex eigenfrequency spectra are illustrated in Figs. 4(b)–4(d) for $\beta = 0$, $\beta = 0.06$, and $\beta = 0.12$, respectively, with the identical geometrical parameters as Fig. 3. In simulations, viscothermal losses have been accounted for, which produce an asymmetry along the imaginary frequency axis. We make two remarks: (1) Although bulk states exist in all three phases, the topological defect state ceases to exist in the \mathcal{PT} symmetry broken phase, but remains observable in the remaining symmetry intact regimes. (2) The pressure

fields distributions of the topological defect states in \mathcal{PT} and \mathcal{APT} symmetric regimes are distinct. In the former phase, the state amplitude displays an oscillating decline away from the defect site as illustrated in the top panel of Fig. 4(b). On the contrary, in the \mathcal{APT} symmetric phase, the pressure undergoes evanescent decay as shown in the top panel of Fig. 4(d). In the experiments, two acoustic sources are placed at sites 1 and -1 (see Supplemental Material Sec. I [25]), and the pressure amplitude in each cavity of the lattice is scanned in a frequency window from 3.22 to 3.58 kHz as shown in Figs. 4(e)–4(g). Within the gap, between the bulk pressure hot spots of Fig. 4(e), a defect localized state is clearly observed at the frequency $f_d = 3356$ Hz, which is the \mathcal{PT} symmetric phase. However, at higher values of the gain-loss contrast ($\beta = 0.06$), in the \mathcal{PT} symmetry broken phase, only extended bulk signatures appear in the spectrum of Fig. 4(f). Last, when symmetry is restored, albeit in the \mathcal{APT} symmetric phase, the strongly confined topological defect state reappears at $f_d = 3344$ Hz as shown in Fig. 4(g). Furthermore, the magnifications of the spatial pressure distributions are displayed in the respective insets, which experimentally accentuates the difference of localization nature. We also demonstrate that the \mathcal{APT} symmetric sonic lattice exhibits stronger sound localization, which is interesting for energy selective waveguiding (see Supplemental Material Sec. VII [25]).

Conclusively, we have predicted and experimentally realized the phase transition among different \mathcal{PT} symmetric phases by utilizing the active CNT films as the non-Hermitian component in a topological acoustic SSH chain. Purely real and complex conjugated two-band dispersions have clearly been observed in the \mathcal{PT} symmetric and \mathcal{APT} symmetric phases, respectively, whose transition across the broken regime is marked by an uneven exceptional line. We have also experimentally characterized the behaviour of symmetry-dependent topological defect states that vanish in the \mathcal{PT} symmetry broken phase, but exhibit damped localization in the \mathcal{PT} and evanescent localization in \mathcal{APT} symmetric regime. Our results provide a feasible platform to study the interaction between non-Hermiticity and topology with special emphasis on this yet unfamiliar \mathcal{APT} symmetric phase, whose fascinating sonic topological signatures have only just been unveiled.

This work was supported by the National Key R&D Program of China (2022YFA1404500 and 2022YFA1404400), NSFC (12074183, 11834008, 12104226, 12227809 and 12225408), Jiangsu Provincial NSF (SBK2023044906) and the Fundamental Research Funds for the Central Universities (020414380181 and 020414380211). Z.Z. acknowledges support from the Funds for Zijin Scholars of Nanjing University. J.C. acknowledges support from the Spanish Ministry of Science and Innovation through a Consolidación Investigadora grant (CNS2022-135706).

*zhangzhiwang@nju.edu.cn

†chengying@nju.edu.cn

‡liuxiaojun@nju.edu.cn

§johan.christensen@imdea.org

- [1] C. M. Bender and S. Boettcher, Real Spectra in Non-Hermitian Hamiltonians Having \mathcal{PT} Symmetry, *Phys. Rev. Lett.* **80**, 5243 (1998).
- [2] R. El-Ganainy, K. G. Makris, D. N. Christodoulides, and Z. H. Musslimani, Theory of coupled optical \mathcal{PT} -symmetric structures, *Opt. Lett.* **32**, 2632 (2007).
- [3] C. E. Rüter, K. G. Makris, R. El-Ganainy, D. N. Christodoulides, M. Segev, and D. Kip, Observation of parity-time symmetry in optics, *Nat. Phys.* **6**, 192 (2010).
- [4] R. Fleury, D. Sounas, and A. Alù, An invisible acoustic sensor based on parity-time symmetry, *Nat. Commun.* **6**, 5905 (2015).
- [5] A. Lupu, H. Benisty, and A. Degiron, Switching using \mathcal{PT} symmetry in plasmonic systems: Positive role of the losses, *Opt. Exp.* **21**, 21651 (2013).
- [6] J. Doppler, A. A. Mailybaev, J. Böhm, U. Kuhl, A. Girschik, F. Libisch, T. J. Milburn, P. Rabl, N. Moiseyev, and S. Rotter, Dynamically encircling an exceptional point for asymmetric mode switching, *Nature (London)* **537**, 76 (2016).
- [7] H. Hodaei, A. U. Hassan, S. Wittek, H. Garcia-Gracia, R. El-Ganainy, D. N. Christodoulides, and M. Khajavikhan, Enhanced sensitivity at higher-order exceptional points, *Nature (London)* **548**, 187 (2017).
- [8] I. Mandal and E. J. Bergholtz, Symmetry and Higher-Order Exceptional Points, *Phys. Rev. Lett.* **127**, 186601 (2021).
- [9] N. Okuma, K. Kawabata, K. Shiozaki, and M. Sato, Topological Origin of Non-Hermitian Skin Effects, *Phys. Rev. Lett.* **124**, 086801 (2020).
- [10] P. Gao, M. Willatzen, and J. Christensen, Anomalous Topological Edge States in Non-Hermitian Piezophononic Media, *Phys. Rev. Lett.* **125**, 206402 (2020).
- [11] M. A. Bandres, S. Wittek, G. Harari, M. Parto, J. Ren, M. Segev, D. N. Christodoulides, and M. Khajavikhan, Topological insulator laser: Experiments, *Science* **359**, eaar4005 (2018).
- [12] B. Hu, Z. Zhang, H. Zhang, L. Zheng, W. Xiong, Z. Yue, X. Wang, J. Xu, Y. Cheng, X. Liu *et al.*, Non-Hermitian topological whispering gallery, *Nature (London)* **597**, 655 (2021).
- [13] T. Liu, Y.-R. Zhang, Q. Ai, Z. Gong, K. Kawabata, M. Ueda, and F. Nori, Second-Order Topological Phases in Non-Hermitian Systems, *Phys. Rev. Lett.* **122**, 076801 (2019).
- [14] Z. Zhang, M. Rosendo López, Y. Cheng, X. Liu, and J. Christensen, Non-Hermitian Sonic Second-Order Topological Insulator, *Phys. Rev. Lett.* **122**, 195501 (2019).
- [15] E. J. Bergholtz, J. C. Budich, and F. K. Kunst, Exceptional topology of non-Hermitian systems, *Rev. Mod. Phys.* **93**, 015005 (2021).
- [16] N. Okuma and M. Sato, Non-Hermitian topological phenomena: A review, *Annu. Rev. Condens. Matter Phys.* **14**, 83 (2023).
- [17] X. Zhang, F. Zangeneh-Nejad, Z. G. Chen, M. Lu, and J. Christensen, A second wave of topological phenomena in photonics and acoustics, *Nature (London)* **618**, 687 (2023).

- [18] Q. Yan, B. Zhao, R. Zhou, R. Ma, Q. Lyu, S. Chu, X. Hu, and Q. Gong, Advances and applications on non-Hermitian topological photonics, *Nanophotonics* **12**, 2247 (2023).
- [19] L. Ge and H.E. Tureci, Antisymmetric \mathcal{PT} -photonic structures with balanced positive and negative index materials, *Phys. Rev. A* **88**, 053810 (2013).
- [20] J.H. Wu, M. Artoni, and G.C. La Rocca, Parity-time-antisymmetric atomic lattices without gain, *Phys. Rev. A* **91**, 033811 (2015).
- [21] P. Peng, W. Cao, C. Shen, W. Qu, J. Wen, L. Jiang, and Y. Xiao, Anti-parity-time symmetry with flying atoms, *Nat. Phys.* **12**, 1139 (2016).
- [22] Y. Choi, C. Hahn, J. W. Yoon, and S. H. Song, Observation of an anti- \mathcal{PT} -symmetric exceptional point and energy-difference conserving dynamics in electrical circuit resonators, *Nat. Commun.* **9**, 2182 (2018).
- [23] A. Bergman, R. Duggan, K. Sharma, M. Tur, A. Zadok, and A. Alù, Observation of anti-parity-time-symmetry, phase transitions and exceptional points in an optical fibre, *Nat. Commun.* **12**, 486 (2021).
- [24] H. C. Wu, L. Jin, and Z. Song, Topology of an anti-parity-time symmetric non-Hermitian Su-Schrieffer-Heeger model, *Phys. Rev. B* **103**, 235110 (2021).
- [25] See Supplemental Material at <http://link.aps.org/supplemental/10.1103/PhysRevLett.131.066601> for (I) numerical simulations, device fabrications, and measurements; (II) derivation of the acoustic Hamiltonian; (III) \mathcal{PT} and \mathcal{APT} symmetries of the non-Hermitian SSH model; (IV) effective lumped-circuit model; (V) topological invariant of the non-Hermitian SSH model; (VI) field distributions of the topological defect states; and (VII) acoustic transmission line based on the non-Hermitian topological defect states, which also include Refs. [26–29].
- [26] M.R. Stinson, The propagation of plane sound waves in narrow and wide circular tubes, and generalization to uniform tubes of arbitrary cross-sectional shape, *J. Acoust. Soc. Am.* **89**, 550 (1991).
- [27] V. Vesterinen, A. O. Niskanen, J. Hassel, and P. Helisto, Fundamental efficiency of nanothermophones: Modeling and experiments, *Nano Lett.* **10**, 5020 (2010).
- [28] H. Arnold and I. Crandall, The thermophone as a precision source of sound, *Phys. Rev.* **10**, 22 (1917).
- [29] R. Süssstrunk and S. D. Huber, Classification of topological phonons in linear mechanical metamaterials, *Proc. Natl. Acad. Sci. U.S.A.* **113**, E4767 (2016).
- [30] F. Yang, Y.-C. Liu, and L. You, Anti- \mathcal{PT} symmetry in dissipatively coupled optical systems, *Phys. Rev. A* **96**, 053845 (2017).
- [31] S. Longhi, \mathcal{PT} symmetry and antisymmetry by anti-Hermitian wave coupling and nonlinear optical interactions, *Opt. Lett.* **43**, 4025 (2018).
- [32] A. Stegmaier, S. Imhof, T. Helbig, T. Hofmann, C. H. Lee, M. Kremer, A. Fritzsche, T. Feichtner, S. Klemmt, S. Höfling *et al.*, Topological Defect Engineering and \mathcal{PT} Symmetry in Non-Hermitian Electrical Circuits, *Phys. Rev. Lett.* **126**, 215302 (2021).
- [33] C. M. Bender, S. Boettcher, and P. N. Meisinger, \mathcal{PT} -symmetric quantum mechanics, *J. Math. Phys. (N.Y.)* **40**, 2201 (1999).
- [34] S.-D. Liang and G.-Y. Huang, Topological invariance and global Berry phase in non-Hermitian systems, *Phys. Rev. A* **87**, 012118 (2013).
- [35] C. Poli, M. Bellec, U. Kuhl, F. Mortessagne, and H. Schomerus, Selective enhancement of topologically induced interface states in a dielectric resonator chain, *Nat. Commun.* **6**, 6710 (2015).
- [36] S. Weimann, M. Kremer, Y. Plotnik, Y. Lumer, S. Nolte, K. G. Makris, M. Segev, M. C. Rechtsman, and A. Szameit, Topologically protected bound states in photonic parity-time-symmetric crystals, *Nat. Mater.* **16**, 433 (2017).